SAMPLING THEORY IN SIGNAL AND IMAGE PROCESSING Vol. 5, No. 1, January. 2006, pp. 21-36

ISSN: 1530-6429

Prolate Spheroidal Wavelet Sampling in Computerized Tomography

G. Walter
Department of Mathematical Sciences, University of Wisconsin–Milwaukee,
P.O. Box 413, Milwaukee, WI 53201-0413, USA
ggw@uwm.edu

T. Soleski
Department of Mathematical Sciences, University of Wisconsin–Milwaukee,
P.O. Box 413, Milwaukee, WI 53201-0413, USA
tigol@uwm.edu

Abstract

In computerized tomography, an image must be recovered from data given by the Radon transform of the image. This data is usually in the form of sampled values of the transform. In this work, a method of recovering the image is based on the sampling properties of the prolate spheroidal wavelets which are superior to other wavelets. It avoids integration and allows the precomputation of certain coefficients. The approximation based on this method is shown to converge to the true image under mild hypotheses. The algorithm is then tested on the standard Shepp–Logan image and shown to be surprisingly good.

Key words and phrases : sampling theory, radon transform, prolate spheroidal wave functions, computerized tomography

2000 AMS Mathematics Subject Classification — 42C40, 94A08, 94A20.

1 Introduction

The prolate spheroidal wave functions (PSWFs) have been an important tool in signal processing for more than forty years. However, they seem to be an inexhaustible and inspirational source of new ideas and methods, both theoretical and applied. Although known as solutions to a Sturm-Liouville problem for more than a century, PSWFs were found by Slepian, Pollak, and Landau to be a solution to a different problem arising in Communication Theory. This was the so-called concentration problem: among all the bandlimited functions find the one with the maximum energy level in a given time interval [11]. Over the years, further extensive studies have produced a number of different ways

to characterize PSWFs, from which many interesting and useful properties of these functions have been derived [6, 7, 12, 13].

Most recently, Walter and Shen [18] have proposed new wavelets based on PSWFs. This wavelet family not only possesses the same maximum energy concentration property, but can also be used in place of the sinc function $S(t) = \frac{\sin \pi t}{\pi t}$ to recover bandlimited signals from their sampled values [17]. The corresponding wavelet scaling function is just the first PSWF with bandwidth π. While these are not orthogonal to their integer translates, they do constitute a Riesz basis of the space of π-bandlimited signals. They do have many desirable analytic properties that other wavelet systems lack.

In applied fields, Shepp and Zhang [10] have used PSWFs to obtain a fast algorithm for recovering a magnetic resonance image (MRI) from its sampled values in the frequency domain. Their prolate wavelets are not the ones considered here, but rather are multidimensional spheroidal wave functions. They were able to show, at least heuristically, that their approach was close to optimal for imaging of brain activity.

Another application involved development of modified high order finite element methods [2] in which the traditional Legendre polynomials have been replaced with PSWFs. They were shown to have considerable potential for use in numerical weather prediction and other applications involving large data sets.

We, in turn, shall use the PS wavelets in computerized tomography (CT), and propose a simple and effective algorithm for reconstructing a good quality image from the projection data collected by a CT scanner. Mathematically, this translates into a problem of recovery of the image function of an object from the sampled values of its Radon transform. To solve this fundamental problem, many wavelet-based methods have been suggested (see [4, 16, 3, 1, 14]). Most of the procedures use two-dimensional wavelets and wavelet transforms; some allow for the use of local data when only a portion of the image is needed. However, none has the combination of good time and frequency response arising with the PS wavelets. Moreover, approximations based on these wavelets retain the analytic properties of the original function, something which no other wavelet systems do.

Our idea is to work with one-dimensional approximations in the Radon transform domain. That allows one to avoid integrations and precalculate many values, thus making the algorithm computationally effective. This is the usual requirement for any procedure that attempts to be somewhat practical. One also must address the fact that PSWFs, in common with most wavelets, do not have a closed form. This makes the need to avoid integrals even more urgent. We achieve it by introducing a procedure that only calls for the values of PSWFs at integers. To find these values we propose an alternative method for computing them without using the traditional Legendre polynomial approximations to PSWFs.

The content of this work is organized as follows. In the next section we summarize the properties of PSWFs and PS wavelets mentioned above, as well as include a quick primer on the mathematical background of CT. Then we describe a reconstruction algorithm based on the properties of PS wavelets. As a part of the procedure a new method for evaluating these functions at integers is introduced. We conclude by presenting some convergence results and computer simulations.

2 Prolate Spheroidal Wavelets and Computerized Tomography

In this section, we list some related properties of the prolate spheroidal wave functions and the associated PS wavelets, as well as give a brief introduction to the subject of computerized tomography.

A. Properties of Prolate Spheroidal Wave Functions

As we attempt to recover an image from the sampled values of its Radon transform, we are naturally interested in bandlimited functions since the frequencies in such an image must be bounded. In particular we work with the space B_π of π -bandlimited functions, i.e., continuous square-integrable functions whose Fourier transforms vanish outside of the interval $[-\pi, \pi]$. According to the Shannon sampling theorem [8], each such function can be represented as

$$f(t) = \sum_k f(k) S(t-k)$$

where $S(t)$ is the sinc function $S(t) = \frac{\sin \pi t}{\pi t}$. Unfortunately, the sinc function has a very slow decay which can make the formula above not adequate for recovering signals with finite time duration.

One of the natural solutions is to consider the set of prolate spheroidal wave functions $\{\phi_n(t)\}$ which form the orthonormal basis of B_π and are highly concentrated in a time interval $[-\tau, \tau]$. These $\{\phi_n\}$ depend on the parameter τ, which we shall, for simplicity, usually assume to be $\tau = 1$, although higher values give greater concentration on the interval.

Here we list some properties of PSWFs each of which can be used as their definition.

1. $\{\phi_n\}$ have maximum energy concentration among all π - bandlimited functions in the interval $[-\tau, \tau]$, i.e., ϕ_0 is the function such that $\int_{-\infty}^{\infty} |\phi_0(t)|^2 dt = 1$ and $\int_{-\tau}^{\tau} |f(t)|^2 dt$ is maximized for $f = \phi_0$; ϕ_1 is the function orthogonal

to ϕ_0 with the same property; ϕ_2 is ...

2. $\{\phi_n\}$ are the eigenfunctions of a differential operator

$$(\tau^2 - t^2)\frac{d^2\phi_n}{dt^2} - 2t\frac{d\phi_n}{dt} + \pi^2 t^2 \phi_n = \mu_n \phi_n, \qquad n = 0, 1, 2, \ldots$$

where μ_n are the eigenvalues.

3. $\{\phi_n\}$ are the eigenfunctions of an integral operator

$$\int_{-\tau}^{\tau} \phi_n(x) S(t-x)dx = \lambda_n \phi_n(t), \qquad n = 0, 1, 2, \ldots$$

We should also mention two more facts about PSWFs that we shall use later:

- each of ϕ_n has exactly n zeroes in the concentration interval $[-\tau, \tau]$;
- the Fourier transform of ϕ_n is given by

$$\widehat{\phi}_n(\omega) = (-1)^n \sqrt{\frac{2\tau}{\lambda_n}} \phi_n\left(\frac{\omega\tau}{\pi}\right) \chi_\pi(\omega),$$

where $\chi_\pi(\omega)$ is the characteristic function of the interval $[-\pi, \pi]$.

The graph of $\phi_0(t)$ is shown in Figure 1 for $\tau = 1$. We shall not use the PSWFs themselves for our approximation, but rather the wavelets based on them.

B. Properties of Prolate Spheroidal Wavelets

The PS-wavelets were introduced in [18] and have as their scaling function $\phi = \phi_0/\widehat{\phi}_0(0)$. It was shown that integer translates of this scaling function $\{\phi(t-n)\}$ form a Riesz basis of the space B_π whatever the value of τ, just as the PSWFs do. By changing the scale by factors of 2, we obtain a *multiresolution analysis* (MRA) $\{V_m\}$ of subspaces of $L^2(\mathbf{R})$, where $f(t) \in V_m$ if and only if $f(2^{-m}t) \in V_0$. An MRA will have the following properties:

1. $\cdots \subseteq V_{m-1} \subseteq V_m \subseteq \cdots \subseteq L^2(\mathbf{R})$,
2. $\overline{\cup V_m} = L^2(\mathbf{R})$,
3. $\cap V_m = \{0\}$.

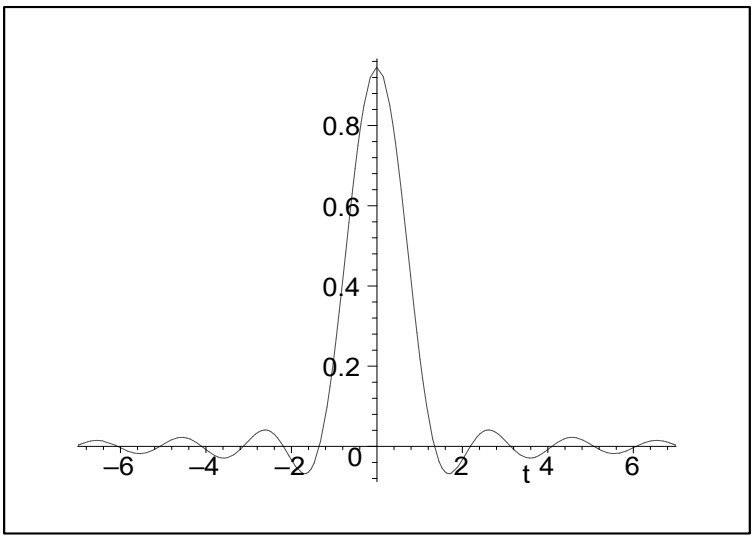

Figure 1: Graph of the prolate spheroidal wave function ϕ_0 in the time domain.

In our case $V_m = B_{2^m\pi}$, the Paley-Wiener space of $2^m\pi-$bandlimited functions; a function f in $L^2(\mathbf{R})$ may be approximated at the scale m by the series approximation of the form

$$f_m(t) = \sum_{n=-\infty}^{\infty} a_{nm}\phi(2^m t - n).$$

Several methods of calculating the coefficents a_{nm} were studied in [18]. One is obtained by using a biorthogonal series and an integral formula. The other, which is the one we shall use here for the most part, avoids integration and uses only the point value $f(2^{-m}n)2^{-m}$ for a_{nm}. Both methods were shown to converge to f uniformly as $m \to \infty$ on the real line for f in an appropriate Sobolev space. The former, however, has a more rapid rate of convergence, whereas the latter avoids Gibbs' phenomenon. This phenomenon, involving the overshoot at points of discontinuity, is present in Fourier appproximation as well as in all standard wavelet approximations. It is particularly troublesome in images since it causes ripple effects at discontinuities of the image. The absence of Gibbs' phenomenon is one reason to use these wavelets in CT.

These PS-wavelets have many other unique properties that make them useful in applications. Their MRA subspaces are closed under differentiation and translation, thereby making them potentially useful for solving differential equations. The parameter τ may be tuned for particular applications. For smaller values of τ, the ϕ's are closer to being orthogonal to their translates and thus easier to work with. For larger values, the energy outside of the concentration

interval $[-\tau, \tau]$ is less, and, in fact, can be made quite small. For example, for $\tau = 2$ the total energy of ϕ outside of the interval is less than $4 \cdot 10^{-5}$. Thus, while ϕ is an entire function which cannot vanish on an interval, for practical purposes it can be taken to be zero outside of the concentration interval whenever τ is sufficiently large.

C. Background on Computerized Tomography

In computerized tomography, the cross-sectional image of an object in the form of a two-dimensional density function is reconstructed from data collected when the object is illuminated by X-ray beams from many different angles. As X-rays pass through the object they are attenuated at different rates by tissues with different densities; measurements obtained at an angle θ are recorded in the form of sampled values of the projection function $P_\theta(t)$. Let $f(x, y)$ denote the density function of the object which is often called the image function, or the object function. Mathematically, the projection function along the line of exposure $t = x \cos\theta + y \sin\theta$ is given by the line integral

$$P_\theta(t) = \iint_{\mathbf{R}^2} f(x, y)\delta(x \cos\theta + y \sin\theta - t)dxdy,$$

where δ is the one-dimensional Dirac delta-function and $P_\theta(t)$ is the Radon transform of $f(x, y)$.

The most common way to recover f from P_θ relies on the Fourier Slice Theorem [5]:

$$\widehat{P}_\theta(\omega) = \hat{f}(\omega \cos\theta, \omega \sin\theta),$$

where $\widehat{P}_\theta$ and $\hat{f}$ denote the Fourier transform of P_θ and f. In other words, the one-dimensional Fourier transform of the projection function gives the two-dimensional Fourier transform of the object function along a radial line. If projections are known at enough angles, the object function can be recovered by using an approximation to the inverse Fourier transform:

$$f(x, y) = \frac{1}{(2\pi)^2} \int_0^\pi \int_{-\infty}^{+\infty} \widehat{P}_\theta(\omega) e^{i\omega(x \cos\theta + y \sin\theta)} |\omega| d\omega d\theta.$$

This is widely known as the backprojection formula

$$f(x, y) = \frac{1}{2\pi} \int_0^\pi Q_\theta(t) d\theta,$$

where $t = x \cos\theta + y \sin\theta$ and Q is the output of a filter with transfer function $|\omega|$, i.e.,

$$\widehat{Q}_\theta(\omega) = \widehat{P}_\theta(\omega)|\omega|,$$

followed by an averaging operator. To make inversion of $\widehat{Q}$ possible, $|\omega|$ is usually multiplied by a smoothing window.

Since $f(x, y)$ has compact support, it cannot be bandlimited at the same time. However, it can belong to a Sobolev space since this would merely require that $\widehat{Q}_\theta(\omega)$ decrease more rapidly than a negative power of ω as $\omega \to \pm\infty$. Such functions, as we have remarked above, can be uniformly approximated by bandlimited functions in $V_m = B_{2^m\pi}$.

3 Reconstruction Algorithm

Our reconstruction procedure is based on the scaling function of PS-wavelet $\phi = \phi_0/\widehat{\phi}_0(0)$. It avoids any Fourier transforms and integrations, and only calls for the values of ϕ_0 at integers. We begin by briefly describing a new linear method for computing such values without using the traditional Legendre polynomial approximation to ϕ_0 [15, 20]. This traditional method first uses the differential operator eigenvalue problem satisfied by the PSWF to estimate the eigenvalue. (This is not the eigenvalue of the integral operator.) Then this eigenvalue estimate is used to estimate the Legendre coefficients of the PSWF, which in turn are used to obtain a Legendre polynomial approximation. This method works on the interval $[-1, 1]$, but has to be modified for values outside of this interval by using a different Bessel function approximation. The new method, on the other hand, provides an entire function approximation on the entire real line.

The most efficient method is to use published tables, but then one is stuck with the Slepian bandwidth values that have been tabulated. Our method involves using a simple MAPLE calculation that any student can do. Details of this method are being published elsewhere, but we include a description for completeness. The algorithm and some convergence results will follow.

A. Discrete Values of PSWFs

Recall that one of the characterizations of PS wave functions is as the maximum of the energy of a signal in a given time interval, i.e., ϕ_0 maximizes

$$E_\tau = \frac{\int_{-\tau}^{\tau} |f(t)|^2 dt}{\int_{-\infty}^{+\infty} |f(t)|^2 dt} \tag{1}$$

among all π -bandlimited functions in space B_π. Since the integer translates $\{S(t-n)\}$ of the sinc function form an orthonormal basis of B_π, solutions of (1) can, by the Shannon sampling theorem [8], be expressed as

$$f(t) = \sum_{n=-\infty}^{\infty} f(n) S(t-n).$$

When this series expansion is used in (1), we obtain E_τ in form of the ratio of

$$\sum_{n=-\infty}^{\infty} f(n) \sum_{k=-\infty}^{\infty} \overline{f(k)} \int_{-\tau}^{\tau} S(t-n)S(t-k)dt \tag{2}$$

to

$$\sum_{n=-\infty}^{\infty} f(n) \sum_{k=-\infty}^{\infty} \overline{f(k)} \int_{-\infty}^{\infty} S(t-n)S(t-k)dt = \sum_{n=-\infty}^{\infty} |f(n)|^2.$$

The former is justified by the dominant convergence theorem while the latter can be obtained when Parseval's equality is applied to the orthonormal sequence $\{S(t-n)\}$ in $L^2(\mathbf{R})$.

Let A_τ denote the doubly infinite matrix that appears in (2), i.e.,

$$A_\tau(i,j) = \int_{-\tau}^{\tau} S(t-i)S(t-j)dt.$$

Then (1) can be expressed as

$$E_\tau = \frac{\langle \boldsymbol{f}, A_\tau \boldsymbol{f} \rangle}{\langle \boldsymbol{f}, \boldsymbol{f} \rangle}$$

where $\boldsymbol{f}$ now denotes a sequence of discrete values $\{f(n)\}$ with the inner product in sense of l^2. To solve this optimization problem, one uses a standard method of operator theory that involves finding the largest eigenvalue λ_τ of the compact, self-adjoint operator A_τ. The eigenvector $\boldsymbol{\phi}$ corresponding to this λ_τ is exactly the vector $\boldsymbol{\phi} = \{\phi(n)\}$ of the values of our PS wave function ϕ_0 at integers satisfying $\|\boldsymbol{\phi}\| = 1$. Of course, in practice the matrix A_τ must be truncated to a finite matrix, which we have found to be quite accurate even with a 15x15 matrix. More details will be found in [19].

B. Algorithm

We approximate the projection function $P_\theta(t)$ by the sampling series at the scale of interest m

$$P_{\theta,m}(t) = \sum_{n=-\infty}^{+\infty} P_\theta(n2^{-m})\phi(2^m t - n) \tag{3}$$

where ϕ is the scaling function of the PS-wavelet introduced in the previous section. In order to avoid any integrations involving ϕ we approximate the filtered projection $Q_\theta(t)$ by the series

$$Q_{\theta,m}(t) = \sum_{k=-\infty}^{+\infty} a_k \phi(2^m t - k) \tag{4}$$

where the coefficients a_k are given by $a_k = \left\langle Q_\theta(t),\, \tilde{\phi}(2^m t - k) \right\rangle$ with $\tilde{\phi}$ being a function biorthogonal to ϕ. Then we have

$$\begin{aligned} a_k &= \frac{1}{2\pi} \left\langle |\omega| \widehat{P}_\theta(\omega),\, 2^{-m} \widehat{\tilde{\phi}}(2^{-m}\omega) e^{-i\omega k 2^{-m}} \right\rangle \\ &= \frac{2^{-2m}}{2\pi} \int_{-\infty}^{+\infty} \left[\sum_n P_\theta(n2^{-m}) \widehat{\phi}(2^{-m}\omega) e^{-i\omega n 2^{-m}} \right] |\omega| \widehat{\tilde{\phi}}(2^{-m}\omega) e^{-i\omega k 2^{-m}} d\omega \\ &= \frac{2^{-2m}}{2\pi} \sum_{n=-\infty}^{+\infty} P_\theta(n2^{-m}) \int_{-2^m\pi}^{2^m\pi} |\omega| e^{-i\omega(n+k)2^{-m}} d\omega \end{aligned} \tag{5}$$

where we used the expansion given in (3) and the fact that $\widehat{Q}_\theta(\omega) = |\omega| \widehat{P}_\theta(\omega)$ and s*upp* $\widehat{\phi} = [-\pi, \pi]$. If we denote the last integral which appears in (6) by $g(n,k)$, i.e.,

$$g(n,k) = 2^{-2m} \int_{-2^m\pi}^{2^m\pi} |\omega| e^{-i\omega(n+k)2^{-m}} d\omega,$$

we obtain for each k

$$a_k = \frac{1}{2\pi} \sum_{n=-\infty}^{+\infty} P_\theta(n2^{-m}) g(n,k).$$

The weight coefficients $g(n,k)$ can be easily found in a closed form:

$$g(n,k) = \begin{cases} \pi^2, & n+k=0 \\ 0, & n+k \text{ is even.} \\ -\frac{4}{(n+k)^2}, & n+k \text{ is odd.} \end{cases} \tag{6}$$

Then the approximation (4) becomes

$$\begin{aligned} Q_{\theta,m}(t) &= \textstyle\sum_k \left[\sum_n P_\theta(n2^{-m}) g(n,k) \right] \phi(2^m t - k) \\ &= \textstyle\sum_n P_\theta(n2^{-m}) b_n(t) \end{aligned} \tag{7}$$

where the weight functions $b_n(t)$ are given by

$$b_n(t) = \sum_{k=-\infty}^{+\infty} g(n,k) \phi(2^m t - k) \tag{8}$$

with $g(n,k)$ as in (6). We switched the order of summation in (7) in order to make the algorithm "implementation friendly," i.e., to be able to begin reconstruction as soon as the first set of projection data becomes available. Note that

the values of b_n are independent of the angle θ and can be precomputed and stored before the procedure begins. Also, the sum in (8) is, in fact, a finite one as $\phi(t)$ essentially becomes zero outside the interval of concentration $[-1, 1]$. Since all points $t_k = 2^m t - k$ at which ϕ needs to be evaluated in (8) are integers, the procedure introduced in a previous subsection can be successfully used.

To recover $f(x, y)$ we recall that $f(x, y) = \frac{1}{\pi} \int_0^\pi Q(x \cos\theta + y \sin\theta) d\theta$. Therefore, we obtain the following approximation to the image function:

$$f(x, y) \approx \frac{1}{2\pi} \sum_{n=-\infty}^{+\infty} \int_0^\pi P_\theta(n2^{-m}) b_n(x \cos\theta + y \sin\theta) d\theta. \tag{9}$$

Since in practice the projection function $P_\theta(t)$ has compact support, the sum in (9) becomes a finite one. Its discrete version used for practical implementation is given by

$$f(x, y) \approx \frac{1}{2\pi} \frac{\pi}{K} \sum_{i=1}^{K} \sum_{n=1}^{N} P_{\theta_i}(n2^{-m}) b_n(x \cos\theta_i + y \sin\theta_i), \tag{10}$$

where N is the number of sample points in each projection, K is the number of views, and θ_i are the angles at which projections have been measured, $i = 1, \ldots, K$. Some sort of interpolation is required as some of the values of $x \cos\theta_i + y \sin\theta_i$ may not coinside with the values of t in (8).

C. Convergence Theorems

We now present some convergence results. We assume they hold under certain smoothness properties of the projection function.

Theorem 1 *Let $P_\theta(t)$ have compact support and $P_\theta(t) \in H^\alpha$ for some $\alpha > \frac{1}{2}$ with $\|P_\theta(t)\|_\alpha \leq C$ for some constant C. Then $P_{\theta,m}(t) \to P_\theta(t)$ uniformly for $\theta \in [0, 2\pi]$ and $t \in \mathbf{R}$ as $m \to \infty$.*

The proof is given in the appendix.

The hypothesis is realistic since real projection data would be expected to be smooth, i.e., $P_\theta(t)$ should be in H^α for $\alpha > \frac{1}{2}$. This follows since discontinuities in $f(x, y)$ would not generally lead to discontinuities in $P_\theta(t)$ because many averaging operations are involved. Real data should be bandlimited since no real process allows arbitrarily large frequencies, but it is frequently corrupted by wideband noise.

Similar results can be obtained for the image function itself approximated by the series (9), but require a greater degree of smoothness. Then under the same hypothesis but with $\alpha > \frac{3}{2}$ we can show the approximation in (9) converges uniformly to $f(x, y)$ as $m \to \infty$ for $(x, y) \in \mathbf{R}^2$.

Figure 2: The actual Shepp–Logan head phantom.

4 Computer Implementation

Our reconstruction algorithm was tested on the well–known Shepp–Logan "head phantom" [9] which is a standard test for the CT algorithms. This image model consists of ten ellipses with various gray levels inside them (Figure 2). As for the regularity of this test image, it has been shown in [14] that it is in the Sobolev space H^α for any $\alpha < 1$.

We generate the filtered projection Q_θ based on (7) at each of N evenly spaced points jT in the interval $[-1, 1]$ where T is a sampling interval, $T = 2^{-m}$, and $j = -\frac{N}{2}, \ldots, \frac{N}{2} - 1$. The weight coefficients b_n as given by (8) are assumed to have been precomputed. We also would like to point to the direct relationship between the scale of interest m and the number N of sampling points. Since the distance T between samples can also be calculated as $T = \frac{2}{N}$, we obtain $N = 2^{m+1}$, i.e., $m = [log_2 N] - 1$. As soon as the values of $Q_{\theta_i}(jT)$ have been obtained, they are used in (10) to reconstruct the object function $f(x, y)$.

The Shepp-Logan head image was reconstructed at two diffrent scales, $m = 6$ and $m = 7$. The latter was the finest scale possible from the given data with $K = 256$ angles and $N = 256$ samples points in each projection (with 256×256 pixels in the image). In the case of the scale $m = 6$, the number of angles, sampling points and pixels was halved. We used linear interpolation for the whole sum in (10). The computer program was written in C++. Figures 3 and

Figure 3: The reconstructed Shepp–Logan image at scale m=6.

4 contain the reconstructed image at the two different scales. We should like to point out that the apparent ripples in Figure 3 are probably less a result of Gibbs' phenomenon than the effect of interpolation.

5 Conclusions

We have introduced an algorithm based on the PS wavelets which avoids integration and uses only precomputed coefficients in the filtering step. It uses a PS wavelet series approximation which reduces excessive oscillations in the reconstructed image. It also uses a new method of numerically calculating the needed values of the PS wavelets which further reduces the computational requirements. This, coupled with the fact that the complexity is no greater than that of traditional methods, should give our algotithm an advantage over them.

The quality of the image in the test cases is as good or better than other methods and differs from the original mainly in that the edges are slightly blurred. Such blurring is expected in any method based on continuous functions, but is more desirable than the ripple artifacts associated with Gibbs' phenomenon that often occur. In the two reconstructed images the one at the coarser scale ($m = 6$) is considerably more blurred than the other and shows the effect of linear interpolartion. This latter effect is largely missing at the finer scale which leads us to conclude that the type of interpolation is not as

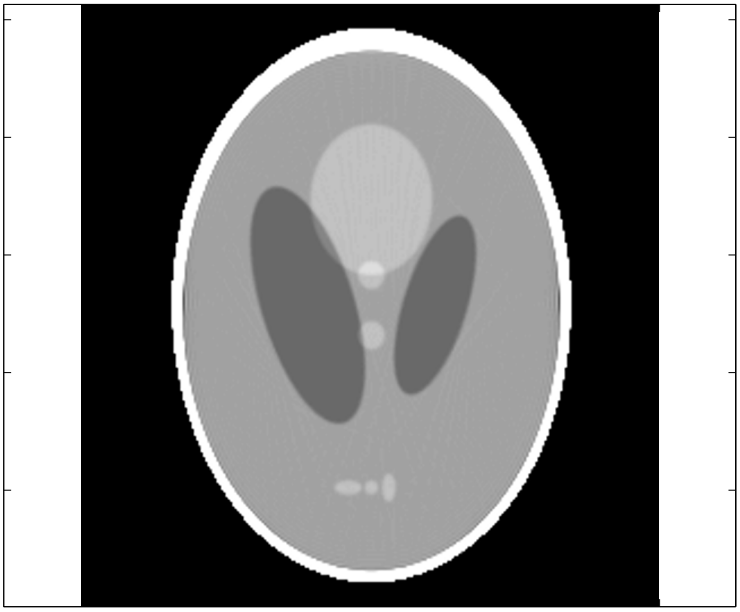

Figure 4: The reconstructed Shepp–Logan image at scale m=7.

important in this method as in others. More work needs to be done to determine if this advantage holds for real data sets arising in CT. The authors are currently attempting to do this and at the same time fine tune the method by incorporating other interpolation methods.

6 Appendix

Proof of Theorem 1 We first estimate the difference between the projection function $P_\theta(t)$ and its approximating series

$$P_{\theta,m}(t) = \sum_{n=-\infty}^{+\infty} P_\theta(n2^{-m})\phi(2^m t - n)$$

in the frequency domain. We have

$$\begin{aligned} \widehat{P}_{\theta,m}(\omega) &= \sum_{n=-\infty}^{+\infty} 2^{-m} P_\theta(n2^{-m})\widehat{\phi}(\omega 2^{-m})e^{-i\omega n 2^{-m}} \\ &= \sum_{k=-\infty}^{+\infty} \widehat{P}_\theta(\omega + 2^{m+1}\pi k)\widehat{\phi}(2^{-m}\omega) \end{aligned}$$

by the Poisson summation formula. Thus, $E = \widehat{P}_{\theta,m} - \widehat{P}_\theta$ has the form $E(\omega) = \widehat{P}_\theta(\omega)[\widehat{\phi}(2^{-m}\omega - 1] + \sum_{k\neq 0} \widehat{P}_\theta(\omega + 2^{m+1}\pi k)\widehat{\phi}(2^{-m}\omega)$. Hence, the integral $\int_{-\infty}^{+\infty} |E(\omega)| d\omega$

satisfies

$$\int_{-\infty}^{+\infty} |E(\omega)|d\omega = \int_{-\infty}^{+\infty} |\widehat{P}_{\theta,m}(\omega) - \widehat{P}_\theta(\omega)|d\omega \leq$$
$$\int_{-\infty}^{+\infty} |\widehat{P}_\theta(\omega)||\widehat{\phi}(2^{-m}\omega) - 1|d\omega + \tag{11}$$
$$\int_{-\infty}^{+\infty} \widehat{\phi}(2^{-m}\omega) \sum_{k\neq 0} |\widehat{P}_\theta(\omega + 2\pi k 2^m)|d\omega.$$

The second integral in (11), since $\widehat{\phi}$ has support in $[-\pi, \pi]$ and is dominated by $\widehat{\phi}(0) = 1$, satisfies

$$\int_{-\pi 2^m}^{\pi 2^m} \widehat{\phi}(2^{-m}\omega) \left(\sum_{k\neq 0} |\widehat{P}_\theta(\omega + 2\pi k 2^m)| \right) d\omega \leq$$
$$\int_{-\infty}^{-\pi 2^m} |\widehat{P}_\theta(\omega)|d\omega + \int_{\pi 2^m}^{+\infty} |\widehat{P}_\theta(\omega)|d\omega.$$

The first integral in (11) is, because of the continuity of $\widehat{\phi}$ near the origin, dominated by

$$\int_{-\infty}^{-2^m\delta} 2|\widehat{P}_\theta(\omega)|d\theta + \int_{-2^m\delta}^{2^m\delta} |\widehat{P}_\theta(\omega)||\widehat{\phi}(2^{-m}\omega) - 1|d\theta + \int_{2^m\delta}^{\infty} 2|\widehat{P}_\theta(\omega)|d\omega.$$

Here δ is the number such that $|\widehat{\phi}(2^{-m}\omega) - 1| < \varepsilon$ for $|2^{-m}\omega| < \delta$ and we have used the fact that $||\widehat{\phi}||_\infty = 1$. The middle integral here is dominated by

$$\varepsilon \int_{-2^m\delta}^{2^m\delta} |\widehat{P}_\theta(\omega)|d\omega < \varepsilon \int_{-\infty}^{\infty} |\widehat{P}_\theta(\omega)| \frac{(\omega^2+1)^{\alpha/2}}{(\omega^2+1)^{\alpha/2}} d\omega \leq$$
$$\varepsilon ||P_\theta||_\alpha \left\{ \int_{-\infty}^{\infty} \frac{1}{(\omega^2+1)^\alpha} d\omega \right\}^{1/2}.$$

Thus, in the limit as $m \to \infty$, each of the terms dominating the two integrals in (11) converges to zero except the last one which is a multiple of ε. This limit is arbitrarily small and hence the conclusion of the theorem follows.

References

[1] C. Berenstein, F. Rashid–Farrokhi, K.J.R. Liu and D. Walnut, Wavelet–Based Multiresolution Local Tomography, *IEEE Trans. Image Proc.*, 6 (1997) 1412–1430.

[2] J. Boyd,, Computation of Grid Points, Quadrature Weights and Derivatives for Spectral Element Methods Using Prolate Spheroidal Wave Functions–Prolate Elements, *ACM Transactions in Computational Logic*, Vol. V, No. N (2004) 1–20.

[3] J. DeStefano and T. Olson, Wavelet Localization of the Radon Transform, *IEEE–SP Int. Symp. Time–Frequency and Time–Scale Analysis*, Victoria, BC, Canada (1992).

[4] M. Holschneider, Inverse Radon Transforms through Inverse Wavelet Transforms, *Inverse Problems*, 7 (1991) 853–861.

[5] A.C. Kak and M. Slaney, *Principles of Computerized Tomographic Imaging*, IEEE Press, New York (1988).

[6] H.J. Landau and H.O. Pollak, Prolate spheroidal wave functions, Fourier analysis and uncertainty, II, *Bell System Tech. J.*, 40 (1961) 65–84.

[7] H.J. Landau and H.O. Pollak, Prolate spheroidal wave functions, Fourier analysis and uncertainty, III, *Bell System Tech. J.*, 41 (1962) 1295–1336.

[8] C.E. Shannon, Communication in the Presence of Noise, *Proc. IRE*, 37 (1949) 10–21.

[9] L.A. Shepp and B.F. Logan, The Fourier Reconstruction of a Head Section, *IEEE Trans. Nucl. Sci.*, NS–21 (1974) 21–43.

[10] L.A. Shepp and C.H. Zhang, Fast Functional Magnetic Resonance Imaging via Prolate Wavelets, *Appl. Comp. Harmonic Anal.*, 9 (2000) 99–119.

[11] D. Slepian, and H.O. Pollak, Prolate spheroidal wave functions, Fourier analysis and uncertainty, I, *Bell System Tech. J.*, 40 (1961) 43–64.

[12] D. Slepian, Prolate spheroidal wave functions, Fourier analysis and uncertainty, IV, *Bell System Tech. J.*, 43 (1964) 3009–3058.

[13] D. Slepian, Some comments on Fourier analysis, uncertainty and modeling, *SIAM Review*, 25 (1983) 379–393.

[14] T. Soleski and G. Walter, The Raised–Cosine Wavelets in Computerized Tomography, *Applicable Analysis*, 83(2) (2004) 199–215.

[15] H. Volkmer, Spheroidal Wave Functions, in *Handbook of Mathematical Functions*, Nat. Bureau of Stds. Applied Math. Series (2004).

[16] D. Walnut, Applications of Gabor and Wavelet Expansions to the Radon Transform, in *Probabilistic and Stochastic Methods in Analysis, with Applications*, J. Byrnes et al., eds., Kluwer Academic Publishers, Boston (1992) 187–205.

[17] G. Walter and X. Shen, Sampling with Prolate Spheroidal Wave Functions, *J. Sampling Theory in Sign. Image Proc.*, 2 (2003) 25–52.

[18] G. Walter and X. Shen, Wavelets Based on Prolate Spheroidal Wave Functions, *J. of Fourier Analysis and Applications*, 10(1) (2004) 1–25.

[19] G. Walter and T. Soleski, A New Friendly Method of Computing Prolate Spheroidal Wavelets , *J. Applied and Computational Harmonic Analysis*, submitted (2004).

[20] H. Xiao, V. Rokhlin and N. Yarvin, Prolate Spheroidal Wave Functions, Quadrature and Interpolation, *Inverse Problems*, 17 (2001) 1–34.